ACS Photonics

Article

pubs.acs.org/journal/apchd5

Entropy-Based Super-Resolution Imaging (ESI): From Disorder to Fine Detail

Idir Yahiatene,*[,†] Simon Hennig,[†] Marcel Müller,[†] and Thomas Huser[†]

[†]Biomolecular Photonics, Department of Physics, University of Bielefeld, Universitaetsstrasse 25, 33615 Bielefeld, Germany

Supporting Information

ABSTRACT: We introduce a novel and universal method for fast optical high, as well as super-resolution imaging. Our method is based on reconstructing super-resolved images from conventional image sequences containing rapid random signal fluctuations. Such sequences could be obtained from either wide-field single-molecule blinking experiments or rapid image sequences with fluorophores undergoing random intensity fluctuations. By calculating the local entropy (H) and cross-entropy (xH) values pixel-by-pixel, weighted with higher order statistics (HOS), a new image with pixel intensities representing the true information content in the time series is obtained. We show that analyzing image sequences by this formalism enables the reconstruction of super-resolved images, where the optical resolution that can be achieved depends only on the number of input frames and the higher order moments used for the calculation. We find that the acquisition of <100 frames per sequence is sufficient to reconstruct super-resolved images of entire cells. We also demonstrate that not only on−off switching of the fluorescent dyes, but also other dynamic events, that is, photobleaching, can be exploited for efficient and high-resolution image reconstructions. This method opens up the potential to obtain super-resolved images from most wide-field fluorescence microscopy systems. By providing a universal Fiji-plugin most users of high-end fluorescence microscopy systems will now benefit from this easy-to-use super-resolution optical microscopy method.

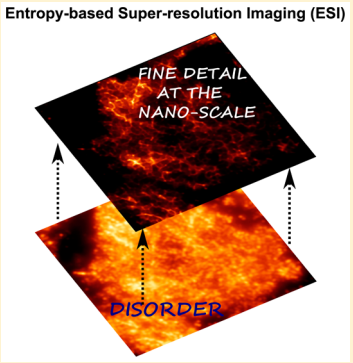

KEYWORDS: *superresolution microscopy, entropy-based superresolution, ESI, fluctuation*

Optical super-resolution microscopy, or nanoscopy, has made a rapid foray into the biomedical sciences, recently culminating in the Nobel prize for Chemistry 2014 being awarded to some of the pioneers of this field.[1] A number of different super-resolution methods have been established during the last 8 years, which can be roughly divided into two different overall approaches. On the one hand, there are direct imaging approaches using optical constraints to achieve a higher spatial resolution, such as stimulated emission depletion (STED)[2−5] and methods based on reassigning photons in confocal microscopy.[6−11] These methods require minimal to no post processing steps to generate images with improved spatial resolution. On the other hand, there are calculation- and localization-based super-resolution methods that take advantage of temporal signal fluctuations, such as superresolution optical fluctuation imaging (SOFI),[12−16] and single molecule localization-based techniques (PALM- and (d)STORM).[17−22] The significantly improved spatial resolution in all these methods is, however, often achieved at a cost. The application of high laser powers or prolonged light exposure necessary to obtain a large number of image sequences lead to photodamage and possibly to an alteration of the sample itself. In addition, long acquisition times typically prevent the investigation of fast dynamic events with few exceptions. Last, but not least, the majority of these techniques require very costly extensions to commercial microscope setups and are not easily achieved by biological users with little to no experience in optical engineering.

Here, we present a new and innovative way to investigate data acquired on conventional fluorescence microscopes, inspired by the SOFI[16] approach to superresolution microscopy. As input data our algorithm accepts short sequences of successively acquired images containing signal fluctuations, for example, data obtained during PALM[18] or STORM[21] experiments, to calculate entropy-weighted higher-order statistics on a pixel-by-pixel basis.[23] We find that just 100 frames per stack are sufficient to reconstruct high-resolution images. The currently most prominent fluctuation-based method, SOFI, works best with emitters exhibiting at least two distinct states similar to fluorescence correlation spectroscopy (FCS) experiments, where dye molecules fluoresce upon entering the confocal laser spot. ESI (entropy-based superresolution imaging) does not require distinct states because (as we show below) it also works well if the fluorescent emitters merely photobleach with time. Additionally, we also observed a certain degree of robustness against out-of-focus contributions of fluorescent emitters. ESI takes the statistical properties of a pixel in an image series into account and calculates its information content[23] (so-called (cross-)entropy values) as well as centralized (joint) higher-order moments to reconstruct a contrast-enhanced as well as resolution-enhanced image by disentangling the information content from molecules to prevent them from overlapping in the reconstructed images.

Received: February 12, 2015
Published: July 14, 2015

DOI: 10.1021/acsphotonics.5b00307
ACS Photonics 2015, 2, 1049−1056

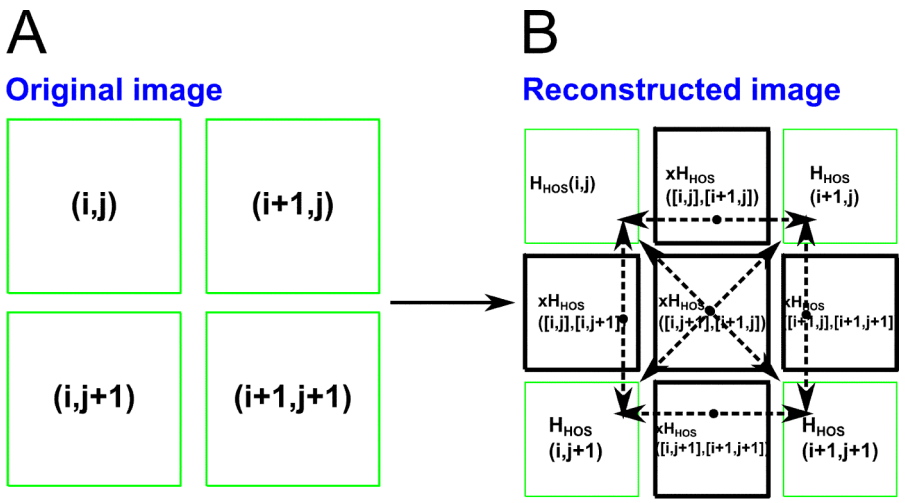

Figure 1. Image formation process in ESI. (A) Pixels of the original image as acquired by a camera with the corresponding coordinates. (B) Resulting image with new intensity values originating from the calculation. Black pixels show intermediate pixels obtained by calculating the cross-entropy and joint higher-order moments between two neighboring pixels. Black bidirectional arrows indicate the camera pixels that serve as inputs for the calculation in order to obtain the highlighted ones.

In the following, we demonstrate the power of ESI and provide detailed instructions on how to utilize ESI and its basic theory to increase the spatial resolution[1] of conventional fluorescence images. We present ESI reconstructions of simulated image sequences, and experimental data, such as the photobleaching[24,25] of 100 nm fluorescent beads, and fixed U2OS cells, where the tubulin cytoskeleton was immunostained by rapidly blinking quantum-dots. A universal plug-in for FiJi written in Java as well as sample input data are provided to ensure widespread reproducibility and application of ESI to similar fluorescence image series obtained by other researchers in the field.

RESULTS AND DISCUSSION: DATA ANALYSIS AND IMAGE RECONSTRUCTION

In the following, we describe the basic idea of the ESI algorithm. For a detailed description of the underlying theory, please see the Supporting Information.

ESI is a method which calculates the information content of an image sequence exhibiting intensity fluctuations or blinking as obtained e.g. during a single-molecule localization-based experiment, such as STORM or PALM.

We then calculate the Shannon-Entropy (H) weighted with (centralized) higher-order moments (HOS = higher order statistics) in a pixelwise manner to reconstruct a higher resolution image from widefield fluorescence data (see Supporting Information).

First, the entropy value is used to identify molecular signals. The interpretation of this idea is depicted in Figure S1 in a picturesque manner. The Shannon-Entropy can be regarded as the expectation value of the information content of a signal. An invariant random variable (or pixel) does not contain information as the value does not change or in other words, the outcome of the experiment is always the same. The information content will increase if the pixel starts adopting a larger number of different intensity values during an image sequence. As an example we consider two pixels I_1 and I_2 taking the values $I_1 = \{1,1,1,1,1,1,1,1,1,1\}$ and $I_2 = \{1,1,5,3,21,7,9,7,8\}$. By directly applying the entropy definition (see eq 1 in the Supporting Information) we obtain $H(I_1) = 0$ for the information content of

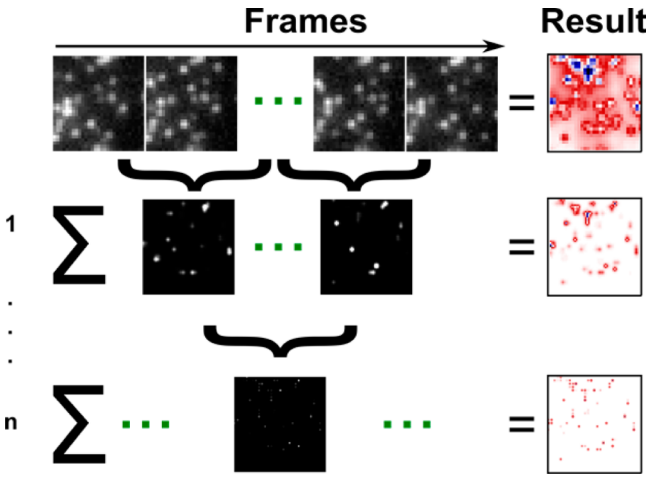

Figure 2. Iterative reconstruction scheme of ESI used to calculate super-resolved images. In each step (1, ..., n) a smaller stack with fewer frames is generated and subsequently processed again as new input. In each iteration a resulting image is calculated as the sum of the entire stack. This loop can be interrupted after each iteration or in case the desired resolution has been reached although it will terminate automatically since the problem obviously reduces continuously. In each step the pixel size will also reduce by a factor of 2, which leads to an increased pixel density and ultimately higher localization precision. The left rectangular box describes the steps performed in the middle, whereas the right column shows the outcome corresponding to each iteration.

I_1 and $H(I_2) \approx 2.31$ in the case of the fluctuating signal in I_2. In this sense we use the entropy to detect molecular events and also to discriminate a fluorescence signal from noise. In this sense one can also readily see that it is less favorable to use pure on/off blinking events, because in this case the number of different intensity values is rather small, although we can successfully reconstruct such data sets as well.

The second factor in the ESI algorithm is the calculation of the centralized moment. Each temporal pixel trace represents a distribution of intensity values. The so-called centralized moments of a distribution depend on their order n (eq 4, Supporting Information). The moments characterize different

DOI: 10.1021/acsphotonics.5b00307
ACS Photonics 2015, 2, 1049−1056

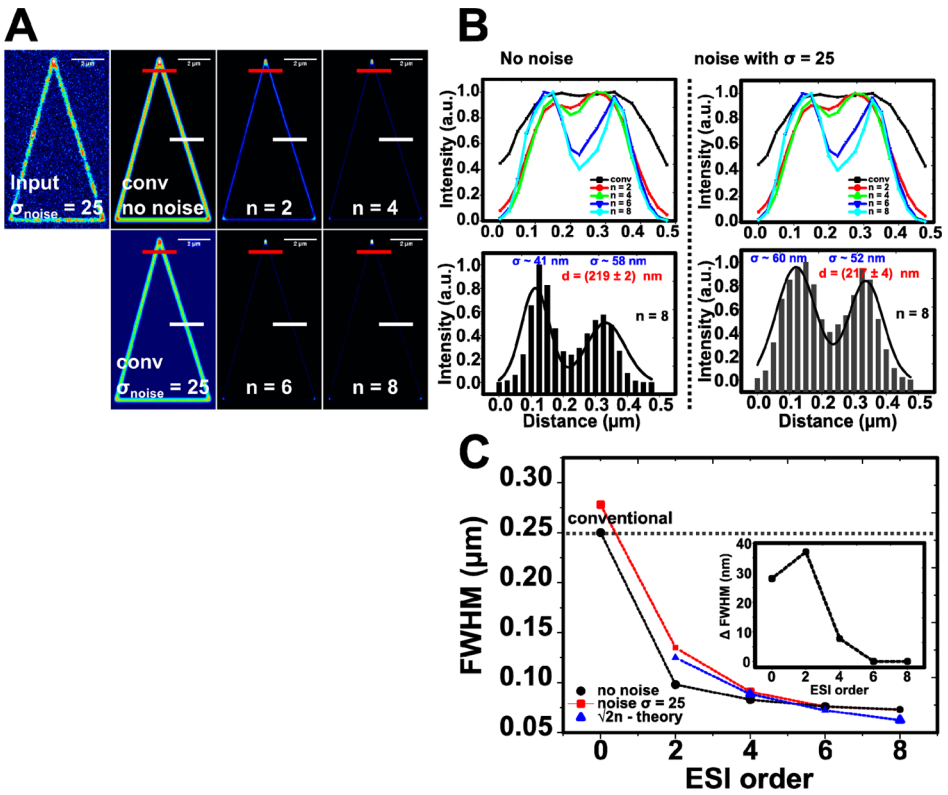

Figure 3. Systematic study of the improvement in lateral resolution that can be achieved by ESI as a function of the order of the centralized moments. (A) Various reconstructions at the first iteration of a simulated triangular structure at different ESI orders. The triangle was captured on a 2000-frame image sequence showing 600 molecular PSFs per frame ensuring that the single emitters are not separated in space at any time. The total number of emitters forming the triangle is 1117. The density of emitters was set to ~50 μm^{-2}. With increasing ESI order the width of the triangle sides decreases by a factor$(2{\cdot}n)^{1/2}$, where n is the order of the centralized moment. The same experiment was performed twice with and without broad Gaussian noise (sd = 25) present. The input data for the noisy and the noiseless case are shown in (A) represented by the first frame of the 2000-frame image sequence. The cross section of the red line in (A) is depicted in the upper graphs of (B). The bar graphs below highlight the cross section taken at eighth order to determine the distance between the two sides of the triangle. The narrowing of the PSF (white line in (A)) as a function of the order is summarized with/without additional noise in (C). The expected loss at low SNR-samples is shown in the inset of (C). The gray dotted vertical line indicates the width considered the classical diffraction barrier at ~250 nm although realistic limits are around 350 nm.

properties of the underlying distribution. Please note that the first moment with $n = 1$ vanishes. The second order moment is the variance of the distribution, whereas the third and the fourth order moments are shape and symmetry related. In an imaging experiment the intensity values represent the optical point spread function (PSF) at different positions. Calculating the moments, or in other words, raising the PSF (which is approximated by a Gaussian density function) to the n-th power leads to a $\sqrt{n}$-fold narrowing of the Gaussian signal with a similar effect as shown in the original SOFI approach published in 2009 by Dertinger et al.

To obtain ESI reconstructed images, first the centralized moment (H_{HOS}, entropy higher-order statistics) is calculated for every original pixel in an image (see Figure 1A).

Then, the product of the cross entropy (xH) and the joint centralized moments of two neighboring pixels is calculated to obtain interpolating information about correlations of the information content between two adjacent original pixels.

Since ESI, as described above, only calculates one additional intermediate pixel between two neighboring pixels, we designed it as an iterative process such, that for each iteration only a defined number of subset frames is processed, as illustrated in Figure 2. For example, an initial image stack of 2000 frames is divided into 100 substacks containing 20 consecutive image frames each. Every substack is then processed separately, resulting in an ESI stack containing 100 reconstructed frames after the first iteration. The next iteration will then use these 100 frames as input data and so on. After each iteration, the number of pixels increases or, in other words, the pixel size is reduced by a factor of 2 in x-,y-direction after each iteration.

All data shown in the following were analyzed using our universal Fiji-Plugin (see Supporting Information), which was efficiently translated to Java from an original custom-coded C++-routine implementing the entire theory described in detail in the SI.

By publishing this work we hope to make fluctuation-based methods for high- and superresolution microscopy more popular and readily available.

DEMONSTRATION OF THE PERFORMANCE OF ESI: SUPER-RESOLUTION IMAGING USING SIMULATED DATA AND DATA OBTAINED FROM SINGLE FLUORESCENT PARTICLES

Computer Simulations. To systematically assess the capabilities of ESI we carried out computer simulations. First, we created a triangular structure composed of 1117 molecular PSFs emitting at a central wavelength of 550 nm and imaged through an objective lens with an NA of 1.49 (Figures 3 and 4). The pixel size for the simulations was set to 50 nm. The pointspread functions have been approximated by a 2D-Gaussian

DOI: 10.1021/acsphotonics.5b00307
ACS Photonics 2015, 2, 1049−1056

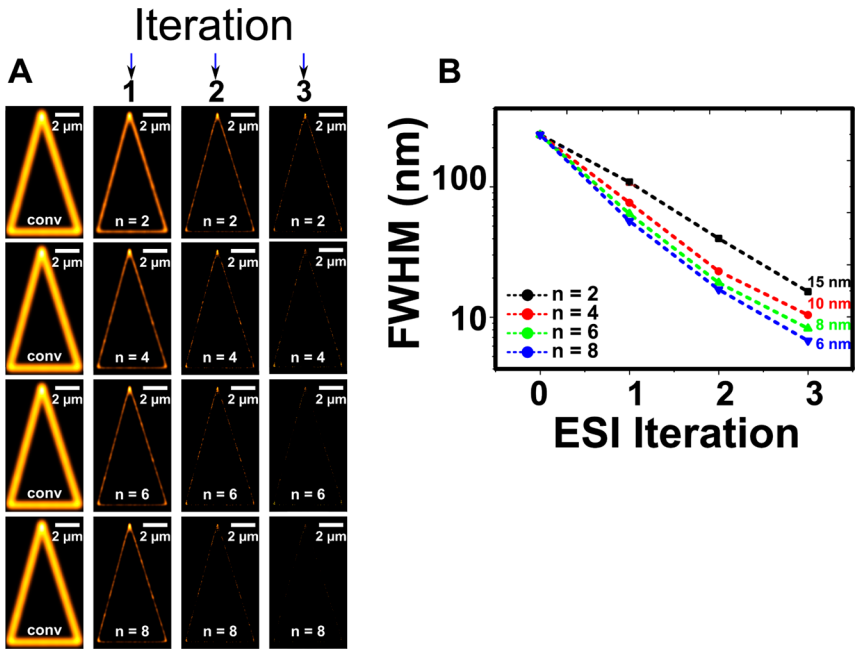

Figure 4. Systematic study of the achievable lateral resolution of ESI as a function of the iterations at a fixed order of the centralized moments. The matrix shown in (A) visualizes reconstructions at constant orders (n = 2, 4, 6, 8) as a function of the iteration (columns) indicated by the blue arrows. In each iteration, three frames of the previous stack are used to reconstruct a single ESI stack used for the next iteration. The initial stack consisting of 2000 frames is reduced to 666 frames after the first iteration (222 frames for the second and 74 after the third iteration). (B) graphically summarizes the fwhm of one side of the triangle as a function of the iteration at constant order (color-coded).

density function $G(x,y) = I_0 \cdot \exp\{-[((x - x_0)^2/2\sigma_x^2) + ((y - y_0)^2/2\sigma_y^2)]\}$, with $\sigma_x = \sigma_y$. The number of photons detected per active molecule per frame was calculated to be ~10000 photons, which nicely matches the molecular brightness of a conventional organic dye at typical acquisition times of ~30−50 ms/frame in STORM/PALM image sequences.

The same simulation was performed by adding a broad Gaussian noise to every pixel of the image sequence with a standard deviation of sd = 25 in order to artificially degrade the signal-to-noise ratio (Figure 3B). For Figures 3 and 4, three original frames are used to reconstruct a single ESI frame if not stated otherwise. In general, the more frames one includes in the analysis, the higher is the probability to reconstruct an emitter.

The left-hand side of Figure 3A shows the widefield reconstruction that is obtained by simply adding up all frames of the image sequence. Starting with this conventional image, we reconstructed images with higher spatial resolution by applying successively higher orders of the centralized moments to weight the Shannon entropy values. Starting with the second ESI order (n = 2) we observe a significant narrowing of the PSFs and the sides of the triangle near the tip become more distinguishable (upper graphs in Figure 3B). The second ESI order effectively decreases the width of the PSF by a factor of 2 according to the theory (see Supporting Information). The second order ESI image truly separates the two sides of the triangle near the tip with and without noise. We finally measure a distance of (219 ± 2) nm in the case of no background and (217 ± 4) nm in the presence of background, as shown in Figure 3B in the dark gray bar graphs. These values compare well to the actual displacement of the molecules of 225 nm that was used to create the simulation. Obviously, the additional background affects the resolution of the algorithm. The distance appears to be smaller, due to the uncertainty introduced by the added noise.

In Figure 3C we quantified the fwhm as a function of the ESI order with and without noise. At higher ESI orders, the width asymptotically converges against a value of ~80 nm well below the optical diffraction limit. Reconstruction at the second or third ESI order readily break the diffraction limit because these orders shrink the PSF by a factor $(2\cdot2)^{1/2} = 2$ and $(2\cdot3)^{1/2} \sim 2.44$, respectively. Please note that the results presented in Figure 3 are limited to the first iteration of the ESI analysis.

The difference in the measured PSF between reconstructions with and without Gaussian noise is depicted in the inset of Figure 3C. At high noise levels, as shown in Figure 3C, the difference drops from ~40 nm to less than 10 nm where the decay is proportional to ~$(1/n)$, with n being the order of the centralized moments.

To further increase the spatial resolution of the ESI reconstructions the resulting stack of the first set of ESI reconstructed images can be processed iteratively multiple times to further gain resolution as schematically depicted in Figure 2. Figure 4A shows a systematic approach to quantify the resolution in the reconstruction that can be achieved in terms of the fwhm of one arm of the simulated triangle. In each row of the image matrix in Figure 4A the ESI order is kept constant while the number of iterations are increased. At higher numbers of iterations (~3) and higher ESI orders the resulting pixel size becomes so small that we observe a nonlinear decrease in contrast (which is also observed in SOFI). In addition to that, by shrinking the width of the PSF the outer parts of the Gaussian distribution resembling the PSF get increasingly dimmer (Figure 4A). As the number of frames decreases with each iteration, also the number of different intensity values in each pixel drops, and therefore, the entropy (average information content) is reduced. After the third iteration the pixel size drops to 6.25 nm. The extreme cases of n = 6 and 8 reduce the width of the PSF to 8 and 6 nm, respectively (Figure 4B). For high ESI

DOI: 10.1021/acsphotonics.5b00307
ACS Photonics 2015, 2, 1049−1056

orders and high numbers of iterations the resulting image becomes more and more pixilated (therefore, less reasonable, because structural information will be lost) due to passing the Nyquist-limit. A very similar effect can also be observed in STORM reconstructions on choosing very small pixel sizes for the rendered image.[19,26,27]

For most practical purposes a reasonable increased spatial resolution and improved image quality can easily be achieved by applying the algorithm twice at second order to reach or even undergo (depending on the sample) the 100 nm threshold. Even a third iteration is realistic at second ESI order. Here one can expect FWHMs of ∼40 nm, comparable to localization precisions achieved in single molecule localization microscopy experiments based on STORM. Please note, however, that in this case ESI only uses 2000 frames in total. At higher label densities (Figures 3 and 4) and fluctuating (not necessarily blinking!) emitters, 20 frames are sufficient for a single reconstruction. The second order enables us to reduce the fwhm of the PSF from ∼250 to 108 nm after the first iteration corresponding to a factor of ∼2.3, confirming the theory (see Supporting Information).

For most (bright) emitters and sample preparations performing the analysis at fourth order twice, an apparent resolution of ∼60 nm can be achieved. The beauty of this technique is that any combination of orders and iterations is possible, enabling one to utilize it to the maximum benefit of either high spatial resolution or high noise suppression.

A comparison of the effects of combinations between the number of iterations and ESI order (n) based on the analysis of the simulated triangle image is shown in Figure 4B.

ESI Reconstruction of 100 nm Fluorescent Beads. In order to initially demonstrate the super-resolution capabilities of ESI on real samples we obtained an image sequence of 100 nm fluorescent beads (Tetraspeck beads, Life Technologies, Inc., Carlsbad, CA) adhered to a glass coverslip surface. This sample also serves as a demonstration of one of the key features of ESI, increasing the spatial resolution of widefield fluorescence data where the only time-dependent change in the fluorescence signal is due to photobleaching (Figure 5E-ii). Using the iterative application of ESI as described above, the widefield projection (represented by a maximum-intensity projection of 5000 frames) shown in Figure 5A is successively enhanced in spatial resolution (B−D), ultimately revealing single beads. The first iteration at fourth ESI order takes the full image sequence into account and already improves the overall intensity distribution leading to a sharper image (see Figure 5B). Figure 5B is the sum of 1000 ESI-frames. Substacks composed of five original images are used to calculate a fourth order ESI image. Subsequently, this 1000-frame stack is again processed at fourth ESI order resulting in a 100-frame stack after the second iteration (10 frames per ESI-image). The result is shown in Figure 5C. Finally, for a sample consisting of well-defined objects (single beads), individual beads can be isolated in the third iteration at second ESI order (see Figure 5E-i). The input data for our ESI routine were recorded on a DeltaVisionlOMXv2 in conventional (widefield) mode using a NA1.42 oil immersion objective. The bead emission was specified to be around 660 nm resulting in a Rayleigh resolution limit of 283.5 nm. After ESI reconstruction, the distance between the two adjacent beads shown in Figure 5Ei is ∼130 nm, indicating ESI's ability to resolve structures well below the diffraction limit.

Super-Resolution ESI Imaging of QD-Labeled U2OS Cells. To demonstrate the performance of ESI reconstructions on biological samples, we recorded time series of widefield fluorescence images from fixed U2OS cells where microtubuli were stained with antibody-capped fluorescent quantum dots. The initial pixel size was set to 170 nm in order to enable fast imaging at ∼20 ms/frame.

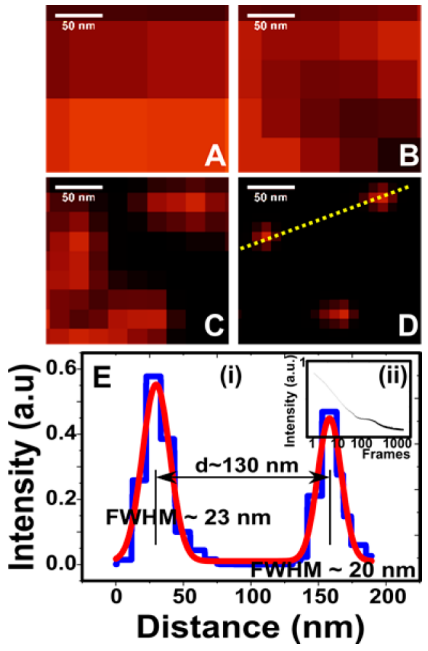

Figure 5. Tetraspeck fluorescent beads with 100 nm diameter adhered to a glass coverslip are used to demonstrate the photobleaching-based ESI reconstruction. (A) Widefield image of the bead surface shown as the sum of the original bead surface consisting of 5000 frames. (B) ESI reconstruction of the first iteration at 4th ESI order. The original stack is reduced to a 1000-frame sequence by generating one ESI image every 5-frames out of the original stack, again shown as a maximum intensity projection. (C) Continued ESI reduction to 100 frames obtained by processing the outcome of (B) at 4th ESI order. A total of 10 frames are used to generate one new ESI image of this 100-frame sequence following the image processing scheme detailed in Figure 2. The remaining 100-frame sequence is finally processed at 2nd order in the 3rd iteration to generate 10 frames resulting in image (D). The cross-section (yellow line) is shown as a line plot in (E-i). The intensity trajectory plotted in (E-ii) demonstrates the exponential nature of the photobleaching process occurring in the sample.

Figure 6 shows micrographs of an entire U2OS cell imaged by widefield fluorescence microscopy and the resulting ESI image in second order reconstruction. Here, the resulting ESI image displays on average an approximately 2-fold increased resolution as can be seen in the adjacent cross sections. In addition, the image contrast has improved as can be seen by the ratio between peaks and valleys in the cross section. A total of 1000 frames are used for the entire analysis although we find that just 200 frames or less are sufficient to reconstruct an ESI image (Figure 6). It is also interesting to note that the signal-to-noise-ratio of the reconstructed images has increased by a factor of 18 compared to the conventional image.[23]

Another example of 2-fold improvement in spatial resolution is shown in Figure 7. Again, the unstained nuclear region is reconstructed with almost zero background. ESI images result in an excellent visualization of the cells' tubulin network structure as can be seen by the magnified views of the corresponding insets to the whole cell images (center row of Figure 7). The width of thin filaments is quantified in intensity cross sections, indicated by the white dotted lines in the magnified inserts.

DOI: 10.1021/acsphotonics.5b00307
ACS Photonics 2015, 2, 1049−1056

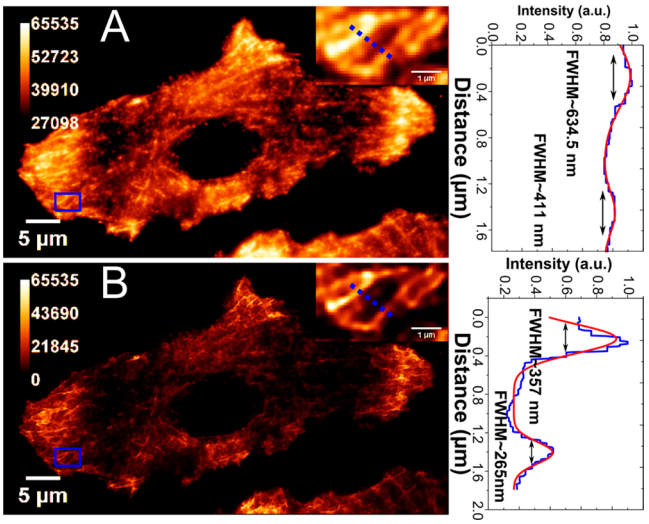

Figure 6. ESI imaging of an entire U2OS cell with microtubules immunostained by fluorescent quantum dots. (A) Widefield image shown as the sum of 1000 frames acquired at 18 ms/frame. (B) ESI reconstruction in the first iteration at 2nd ESI order using 5 frames, resulting from packing 200 frames into one single ESI-frame. It exhibits a 2-fold increase in (apparent) resolution on average, as demonstrated by the narrowing of filaments in the cross sections plots corresponding to (A) and (B) shown on the right-hand side of the figure. Red lines depict bimodal Gaussian fits.

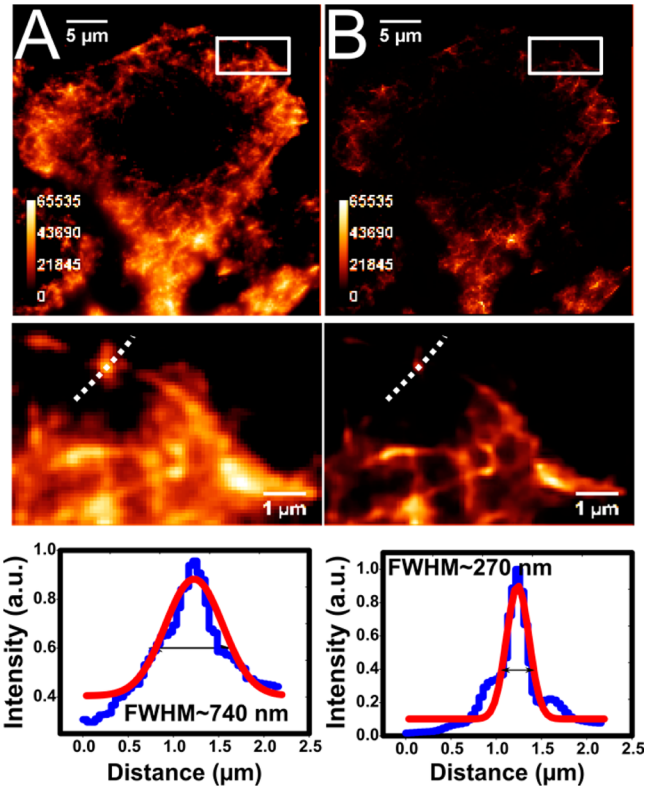

Figure 7. Another example of an entire U2OS cell imaged by ESI. (A) Widefield projection image composed of the sum of 1000 frames and (B) corresponding ESI reconstruction at 2nd order as a sum of 50 resulting ESI frames are shown. The magnified images displayed in the middle row correspond to the blue rectangles in the figures. In order to demonstrate the narrowing of structures after ESI reconstruction the line plots in the last row show the cross sections indicated by the white dotted lines along a filament within the cell.

Gaussian approximations (red curves) show that the width of the filaments has significantly narrowed. We also find that ESI efficiently removes out-of-focus contributions. Therefore, all the filaments surrounding the nucleus become visible at high contrast while out-of-focus contributions are suppressed. This ability makes it perfectly suitable for 3D imaging as well.

As true resolution enhancement can only be judged by resolving two objects that are separated by a distance less than the diffraction limit of the microscope, we choose a region in Figure 8 highlighted by the white box, which contains two

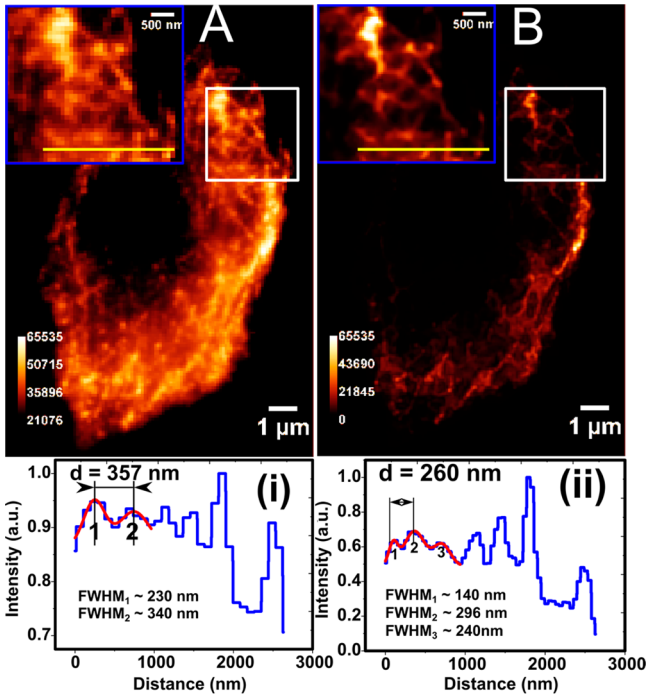

Figure 8. Super-resolution imaging by ESI reconstruction. (A) conventional image of an immunostained U2OS cell after acquisition of a 1000-frame image sequence at 18 ms/frame. (B) Second-order ESI reconstruction at 10 original frames per ESI-frame resulting in a 100-frame ESI-stack. The white region of interest (ROI) shown in the blue box in the upper left corner of (A) and (B) highlights an area which nicely demonstrates the improved spatial resolution. The cross section along the yellow line is depicted in (i) and (ii) corresponding to the lines in (A) and (B). Within the first 1000 nm the original two peaks indicating tubulin filaments (A-i) break up into three peaks (B-ii). The distance of these two separated filaments is determined to be 260 nm, which is just below the theoretical diffraction limit of ~270 nm determined in the text. The FWHMs of the peaks quantify the apparent resolution showing a tremendously increased degree of detail.

filaments with a distance of approximately 260 nm, just slightly below the theoretical diffraction limit of 268.2 nm (although we obtained an experimental value of ~370 nm). The theoretical limit is obtained by applying the Rayleigh-criterion at a wavelength of 655 nm (quantum-dot emission) and for an oil-immersion objective lens with a numerical aperture of 1.49. It turns out that the initial filament shown at 250 nm in the cross-section of the widefield image, splits into two filaments at around 100 and 360 nm in the ESI reconstruction (bottom art of Figure 8). In addition, the width of the filaments reduces to $\sigma \sim 60$ nm (corresponding to a fwhm of 140 nm).

Lastly we demonstrate the iterative ESI analysis process on U2OS cells as a means to successively decrease the width of structures (which, ultimately could be used to improve

DOI: 10.1021/acsphotonics.5b00307
ACS Photonics 2015, 2, 1049−1056

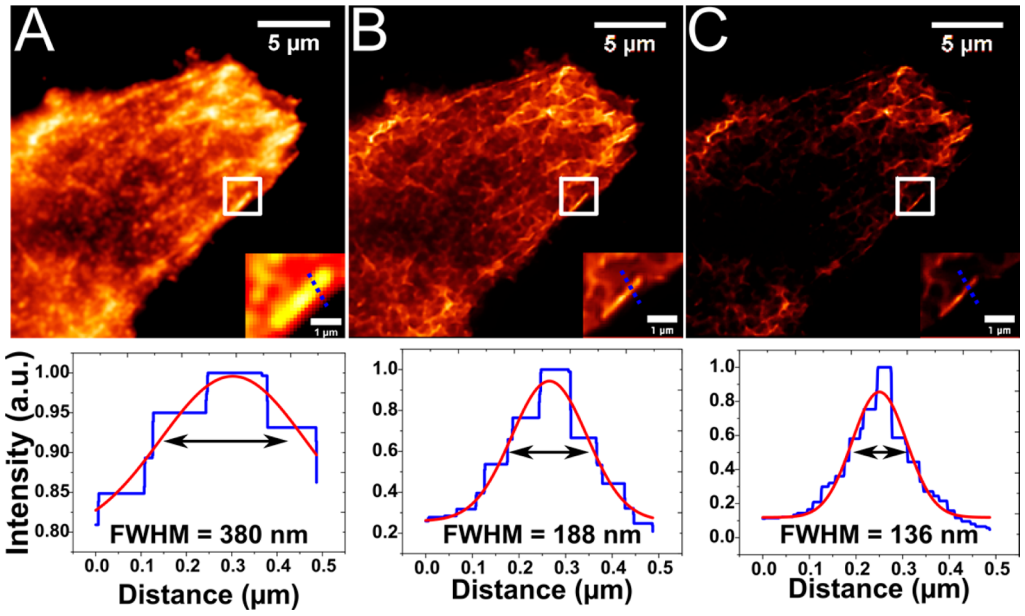

Figure 9. U2OS cell immunostained for tubulin using quantum dots. A reduction of filament size well below the diffraction limit can be seen after just two ESI iterations. (A) Sum of 1000 frames acquired at 18 ms/frame. (B) ESI reconstruction of (A) at second ESI order exhibiting a 2-fold increase in (apparent) resolution on average. (B) represents a sum over 100 ESI-frames after the first iteration. (C) shows the iteratively processed stack of (B) as a sum of 10 frames at first ESI order. The white squares indicate magnified areas depicted as insets and the dashed lines correspond to the cross sections at the bottom of the figure.

localization precision). Figure 9A depicts the widefield representation of yet another QD-stained U2OS cell. Figure 9B,C show the first and second ESI iteration at second (2-fold improvement) and first ESI order ($\sqrt{2}$-fold improvement), respectively. Here, the width of individual filaments reduces to ∼136 nm. The initial stack is successively shortened from 1000 initial frames to 10 frames in the last step. In each iteration only 10 frames of the previous step were used to reconstruct one ESI frame. Here, again, we would like to stress the relevance for live-cell applications.

Experimental. Preparation of Bead Surface. The Tetraspeck (Life Technologies, Carlsbad, CA, U.S.A.) stock solution containing 100 nm fluorescent beads was diluted 1:1000 in distilled water and simply allowed to dry on a clean coverslip surface and subsequently imaged in widefield-mode of a DeltaVision|OMX v2.0 (GE Healthcare, Amersham, U.K.) at 50% laser power (corresponding to an absolute power of ∼4 mW behind the objective lens) and an acquisition time of 50 ms/frame.

U2OS Staining Protocol. U2OS cells were plated in LabTek chambered coverglass, Nunc (8-well) for 24−36 h. Fixation of the cells was carried out with 4% prewarmed paraformaldehyde (Sigma) for 10 min. After fixation, the cells were washed 3 times with phosphate buffered saline (PBS) (Cat. No. P4417, Sigma-Aldrich) containing 0.1% (w/v) Tween and subsequently permeabilized with 0.3% triton X-100 (Cat. No. X100−5 ML, Sigma-Aldrich) for 10 min. After additional washing with PBS for 3 times, cells were blocked with 1% w/v bovine serum albumin (BSA; Cat. No. A7906−10G, Sigma-Aldrich) solved in PBS for 30 min, at room temperature followed by the additional washing steps. Next 250 μL antitubulin antibody (Cat. No. T8328, Sigma-Aldrich) was added at a concentration of 20 μg/mL and incubated for 60 min at room temperature with subsequent washing with PBS. A total of 250 μL at 2 μg/mL Qdot655-anti mouse secondary antibody (Q11021MP, Life Technologies) were added and incubated overnight at 4 °C, followed by washing steps.

Conclusions. In this publication we introduce a novel technique for rapid super-resolution fluorescence imaging relying on pixelwise calculation of entropy-weighted higher-order statistics. We demonstrate the reconstruction of images with improved spatial resolution and contrast, reconstructed from fluctuating emitters acquired in image sequences as typically obtained in single molecule localization microscopy. ESI, however, does not strictly require discrete intensity states (on/off). It can exploit any photophysical state of a fluorescent emitter which leads to an intensity fluctuation to gain information about the sample's dynamic behavior and to reconstruct higher resolution images. We demonstrated that even a nonreversible process such as photobleaching can be used to localize emitting structures, such as fluorescent beads. On biological samples we have been able to achieve apparent resolutions of $\sigma \sim 59$ nm (fwhm ∼ 140 nm) with Quantum-Dot-stained U2OS cells well below the optical diffraction limit. We have also provided evidence that ESI reconstructions can achieve even further improved spatial resolution of less than 100 nm if performed with organic dye molecules.

Because of the low number of input frames required for successful ESI reconstructions, highly dynamic intracellular processes should become observable in future applications. ESI-based super-resolution imaging should, under optimized conditions, be able to compete with popular super-resolution methods, even at video rate. Based on its mathematically fairly simple and iterative implementation, it should be straightforward to extend ESI for massive parallelization, resulting in quasi-instantaneous super-resolution imaging during the experiment. By adapting this method to a graphics processor unit (GPU) platform, we expect a 50−100-fold increase in reconstruction speed and therefore the method is only limited by the camera acquisition and read-out time. In addition, ESI is readily expandable to 3D imaging by acquiring images from multiple vertical planes and subsequent reconstruction of each plane.

DOI: 10.1021/acsphotonics.5b00307
ACS Photonics 2015, 2, 1049−1056

Furthermore, we would like to stress the tremendous simplicity of ESI which should make it available to any scientist using conventional widefield microscopes. A Fiji-plugin written in Java and a short users guide to perform this analysis can be found in the Supporting Information.

■ ASSOCIATED CONTENT

Supporting Information

A brief and clear manual of the Fiji-Plugin published with this paper and theoretical derivations for the present work. The Supporting Information is available free of charge on the ACS Publications website at DOI: 10.1021/acsphotonics.5b00307.

■ AUTHOR INFORMATION

Corresponding Author

*E-mail: iyahiate@physik.uni-bielefeld.de. Tel.: +49 521 106-5450.

Notes

The authors declare no competing financial interest.

■ ACKNOWLEDGMENTS

This work was supported by the German Academic Exchange Service (DAAD), Grant No. 50722682. We would like to thank Saskia Bannister for U2OS cell preparation.

■ REFERENCES

(1) Abbe, E. Beiträge zur Theorie des Mikroskops und der mikroskopischen Wahrnehmung. *Archiv für mikroskopische Anatomie* **1873**, *9*, 413−468.

(2) Loew, L. M.; Hell, S. Superresolving dendritic spines. *Biophys. J.* **2013**, *104*, 741−3.

(3) Vicidomini, G.; Schönle, A.; Ta, H.; Han, K. Y.; Moneron, G; Eggeling, C.; Hell, S. W. STED nanoscopy with time-gated detection: theoretical and experimental aspects. *PLoS One* **2013**, *8*, e54421.

(4) Hell, S. W. Far-Field Optical Nanoscopy. *Science* **2007**, *316*, 1153−1158.

(5) Hell, S. W.; Wichmann, J. Breaking the diffraction resolution limit by stimulated emission: stimulated-emission-depletion fluorescence microscopy. *Opt. Lett.* **1994**, *19*, 780−782.

(6) Winter, P. W.; York, A. G.; Nogare, D. D.; Ingaramo, M.; Christensen, R.; Chitnis, A.; Patterson, G. H.; Shroff, H. Two-photon instant structured illumination microscopy improves the depth penetration of super-resolution imaging in thick scattering samples. *Optica* **2014**, *1*, 181−191.

(7) York, A. G.; Chandris, P.; Nogare, D. D.; Head, J.; Wawrzusin, P.; Fischer, R. S.; Chitnis, A.; Shroff, H. Instant super-resolution imaging in live cells and embryos via analog image processing. *Nat. Methods* **2013**, *10*, 1122−1126.

(8) Heintzmann, R.; Ficz, G. Breaking the resolution limit in light microscopy. *Briefings Funct. Genomics Proteomics* **2006**, *5*, 289−301.

(9) Roth, S.; Sheppard, C.; Wicker, K.; Heintzmann, R. Optical photon reassignment microscopy (OPRA). *Opt. Nano.* **2013**, *2*, 5.

(10) De Luca, G. M.; Breedijk, R. M.; Brandt, R. A.; Zeelenberg, C. H.; de Jong, B. E.; Timmermans, W.; Azar, L. N.; Hoebe, R. A.; Stallinga, S.; Manders, E. M. Re-scan confocal microscopy: scanning twice for better resolution. *Biomed. Opt. Express* **2013**, *4*, 2644−56.

(11) Muller, C. B.; Enderlein, J. Image scanning microscopy. *Phys. Rev. Lett.* **2010**, *104*, 198101.

(12) Dedecker, P.; Mo, G. C.; Dertinger, T.; Zhang, J. Widely accessible method for superresolution fluorescence imaging of living systems. *Proc. Natl. Acad. Sci. U. S. A.* **2012**, *109*, 10909−14.

(13) Dertinger, T.; Colyer, R.; Vogel, R.; Heilemann, M.; Sauer, M.; Enderlein, J.; Weiss, S. Superresolution optical fluctuation imaging (SOFI). *Adv. Exp. Med. Biol.* **2012**, *733*, 17−21.

(14) Dertinger, T.; Heilemann, M.; Vogel, R.; Sauer, M.; Weiss, S. Superresolution optical fluctuation imaging with organic dyes. *Angew. Chem., Int. Ed.* **2010**, *49*, 9441−9443.

(15) Dertinger, T.; Colyer, R.; Vogel, R.; Enderlein, J.; Weiss, S. Achieving increased resolution and more pixels with Superresolution Optical Fluctuation Imaging (SOFI). *Opt. Express* **2010**, *18*, 18875−85.

(16) Dertinger, T.; Colyer, R.; Iyer, G.; Weiss, S.; Enderlein, J. Fast, background-free, 3D super-resolution optical fluctuation imaging (SOFI). *Proc. Natl. Acad. Sci. U. S. A.* **2009**, *106*, 22287−92.

(17) Yahiatène, I.; Aung, H. H.; Wilson, D. W.; Rutledge, J. C. Single-molecule quantification of lipotoxic expression of activating transcription factor 3. *Phys. Chem. Chem. Phys.* **2014**, *16*, 21595−21601.

(18) Shroff, H.; White, H.; Betzig, E. Photoactivated Localization Microscopy (PALM) of adhesion complexes. *Curr. Protoc. Cell Biol.* **2013**, *58*, 4.21.1−4.21.28.

(19) Wolter, S.; Löschberger, A.; Holm, T.; Aufmkolk, S.; Dabauvalle, M. C.; van de Linde, S.; Saur, M. rapidSTORM: accurate, fast open-source software for localization microscopy. *Nat. Methods* **2012**, *9*, 1040−1041.

(20) van de Linde, S.; Löschberger, A.; Klein, T.; Heidbreder, M.; Wolter, S.; Heilemann, M.; Sauer, M. Direct stochastic optical reconstruction microscopy with standard fluorescent probes. *Nat. Protoc.* **2011**, *6*, 991−1009.

(21) Rust, M. J.; Bates, M.; Zhuang, X. Sub-diffraction-limit imaging by stochastic optical reconstruction microscopy (STORM). *Nat. Methods* **2006**, *3*, 793−795.

(22) Betzig, E.; Patterson, G. H.; Sougrat, R.; Lindwasser, O. W.; Olenych, S.; Bonifacino, J. S.; Davidson, M. W.; Lippincott-Schwartz, J.; Hess, H. F. Imaging intracellular fluorescent proteins at nanometer resolution. *Science* **2006**, *313*, 1642−5.

(23) Yahiatene, I.; Hennig, S.; Huser, T. Optical fluctuation microscopy based on calculating local entropy values. *Chem. Phys. Lett.* **2013**, *587*, 1−6.

(24) Cox, S.; Rosten, E.; Monypenny, J.; Jovanovic-Talisman, T.; Burnette, D. T.; Lippincott-Schwartz, J.; Jones, G. E.; Heintzmann, R. Bayesian localization microscopy reveals nanoscale podosome dynamics. *Nat. Methods* **2011**, *9*, 195−200.

(25) Gordon, M. P.; Ha, T.; Selvin, P. R. Single-molecule high-resolution imaging with photobleaching. *Proc. Natl. Acad. Sci. U. S. A.* **2004**, *101*, 6462−5.

(26) Loschberger, A.; Franke, C.; Krohne, G.; van de Linde, S.; Sauer, M. Correlative super-resolution fluorescence and electron microscopy of the nuclear pore complex with molecular resolution. *J. Cell Sci.* **2014**, *127*, 4351−5.

(27) Wolter, S.; Schuttpelz, M.; Tscherepanow, M.; van de Linde, S.; Heilemann, M.; Sauer, M. Real-time computation of subdiffraction-resolution fluorescence images. *J. Microsc.* **2010**, *237*, 12−22.

DOI: 10.1021/acsphotonics.5b00307
ACS Photonics 2015, 2, 1049−1056